Electronic Supplementary Material (ESI) for Physical Chemistry Chemical Physics.

Understanding the influence of disorder on the exciton dynamics and energy transfer in Zn-phthalocyanine H-aggregates

Supporting Information

Experimental 2D electronic spectroscopy setup, acquisition and data analysis

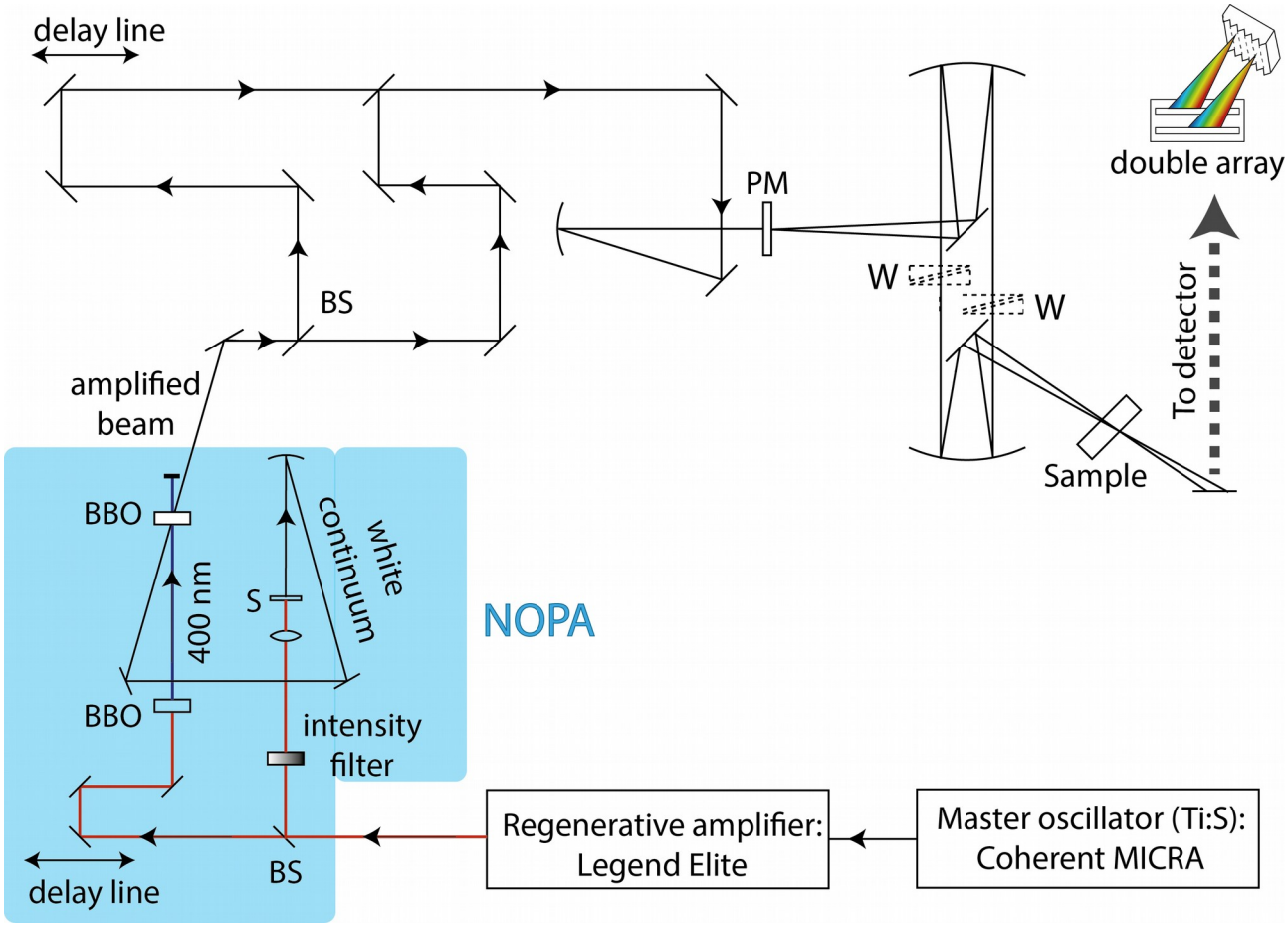

Figure S1. *Experimental setup used for 2D electronic spectroscopy and broadband pump-probe measurements. The pulses coming from the master oscillator Coherent MICRA are amplified by the regenerative amplifier Coherent LEGEND ELITE are then sent to the Non-Collinear Optical Amplifier (NOPA), which produces ultrafast pulses tunable between 500 and 800 nm. Two beam*

splitter (BS) in sequence generate the reference beam first and then separate pump and probe. The time delay between the two beams is controlled by a motorized delay line. Pump and probe cross a Phase Mask (PM) generating two identical copies for each incoming beam. The four beams are then collimated and focused in the sample (Box-Car geometry). Two couples of wedges (W) are placed in the pumps path in order to finely control their relative delay.

The 2D electronic spectroscopy setup is shown in Fig. S1. The main oscillator is a self-mode locking Ti:Sapphire laser (Coherent Micra), producing pulses centered at 810 nm, 85 nm bandwidth and 400 mW power at 89 MHz repetition rate. The beam then goes through a regenerative amplifier (Coherent Legend Elite) that involves three steps: stretching, amplification and compression. The output is a broadband pulse centered at 800 nm, 35 fs duration, 1 KHz rep. rate, 3 mJ of energy per pulse. The polarization of the beam is rotated from horizontal to vertical and sent to a Non-Collinear Optical Parametric Amplifier (NOPA) [1]–[3]; if necessary, a chopper synchronized at a fraction of the 1 KHz repetition rate can be inserted to reduce the power reaching the NOPA. The advantage of using a non-collinear parametric amplifier is that, with BBO amplifying crystal cut at the proper angle (roughly 31° from the optical axis), phase matching can be achieved in a frequency range much broader than in the collinear case [1]. In this way very broad-band pulses in the green-red region of the spectrum can be obtained. In order to produce the desired visible pulses through the NOPA, the 800 nm incoming beam is first split into two arms of very different intensities. One is very weak; it is tightly focused onto a Sapphire plate to generate white continuum that acts as the seed pulse. The more intense part is frequency doubled to 400 nm in a BBO crystal to produce the pump beam. The white light continuum pulse is purposely chirped in a thin glass plate and sent to the parametric crystal, where it overlaps the 400 nm pump pulse. The delay between the chirped seed pulse and the pump pulse determines the color of the NOPA output. The overall parametric amplification process introduces a substantial chirping in the amplified output. In order to compensate for the dispersive optics employed, a couple of Dispersing Compensating Mirrors (DCM10 from Veneteon®), or chirped mirrors, are used (Fig. S3a). They consist in multi-dielectric layers, each one reflecting a different spectral interval so that, after an appropriate number of reflections, the phase dispersion throughout the entire spectrum of the pulse is canceled. The negative dispersion introduced by the DCM mirrors can be controlled by adjusting the number of reflections between the two mirrors. After passing this device, typical pulses are 13 fs long. The pulse characterization has been performed by recording and fitting the cross correlation intensity, as fully described in ref. [4]. In Fig. S2a the cross correlation intensity profile is plotted with respect to

the frequency. The filled square symbols are the experimental data, the solid red curve is the reconstructed fit with sech2 profile. The FWHM of the cross correlation is 19 fs, corresponding to a pulse duration of approximately 13 fs. This pulse duration is still longer than the transform limited value for such a broad band. As reported in the literature, this limit can be approached by using active optics (like pulse shaper) or passive optics (i.e. DCMs) specially designed for the actual dispersion of the set-ups. The compression reached in Fig. S2b is enough for our purpose.

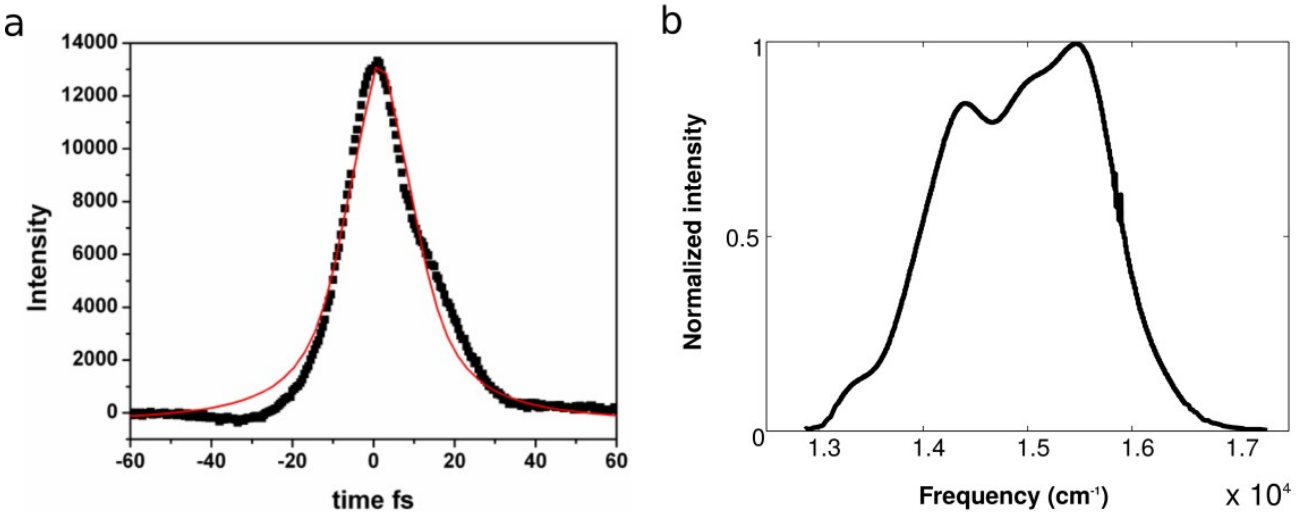

Figure S2. *a) Cross correlation experimental data for the broadest band amplified with the NOPA (square dots). In red is superimposed the fit with sech2 profile. b) Amplified pulse spectra obtained after the NOPA output. The FWHM of the spectra is approximately 2000 cm^{-1}.*

The NOPA output is sent through two beam-splitters in sequence, which generate first the reference pulse and then separate pump and probe. The pump goes through a delay line that controls the population time τ_2. Both the pump beams are aligned on the same vertical plane and then focused by a spherical mirror onto a Phase Mask (PM), which is a refractive optics optimized to have maximum intensity at the orders ±1. For each incoming beam, the phase mask generates two replicas (slightly dispersed) propagating in the horizontal plane. In total 4 beams in the boxcar geometry are first collimated and then focused into the sample by a couple of spherical mirrors. The non-linear signal produced by beams E1-3 propagates in the same direction of the fourth beam, acting as Local Oscillator (LO), and allowing heterodyne detection. In fact, the intensity of the emitted signal is generally too low to be detected in homodyne mode.

In order to control the relative delay τ_1 between the two pumps, each of the beams E1 and E2

crosses a couple of fused silica wedges in the configuration shown in Fig. S3b. The wedges have linearly variable thickness from 2 to 1.4 mm. The timing of each beam is controlled by moving one of two wedges by means of a motorized stage (M 112.1DG Phisik Instrumente); the presence of two wedges with parallels surfaces compensate the deviation of the beam. With this method, very high temporal resolution is achieved: the bidirectional reproducibility of our stage is 0.1 µm, meaning that the precision on the positioning of the wedges and, consequently on the delay between E1 and E2 is 3 as. During a 2D scan, the delay step is set to 0.25 fs, corresponding to a translation of 6.25 µm. The dispersion acquired by the E1 and E2 beams crossing the wedges is matched in the other two beams by means of two couple of fixed wedges. Furthermore, E_{LO} is delayed with respect to E3 of about 300 fs, so that it does not interfere with the non-linear effects produced by the other three beams. With this scheme, the only spurious signal superimposed to the echo and transient grating signal is the E3-LO pump-probe. It can be easily isolated and removed from the proper signal, as we will see in the data treatment section. The signal collection is performed through a monochromator (Horiba Jobin Yvon R CP 140 1602, 16.8 nm/mm average dispersion, optimal spectral range 285-715 nm) coupled with a detector. The detector consists of two NMOS (Hamamatsu) arrays of 256 pixels, one for the echo signal interfering with the LO, and one for reference beam. The entire acquisition system, including electronics for read-out of the arrays, signal amplification, data digitalization and treatment is homemade.

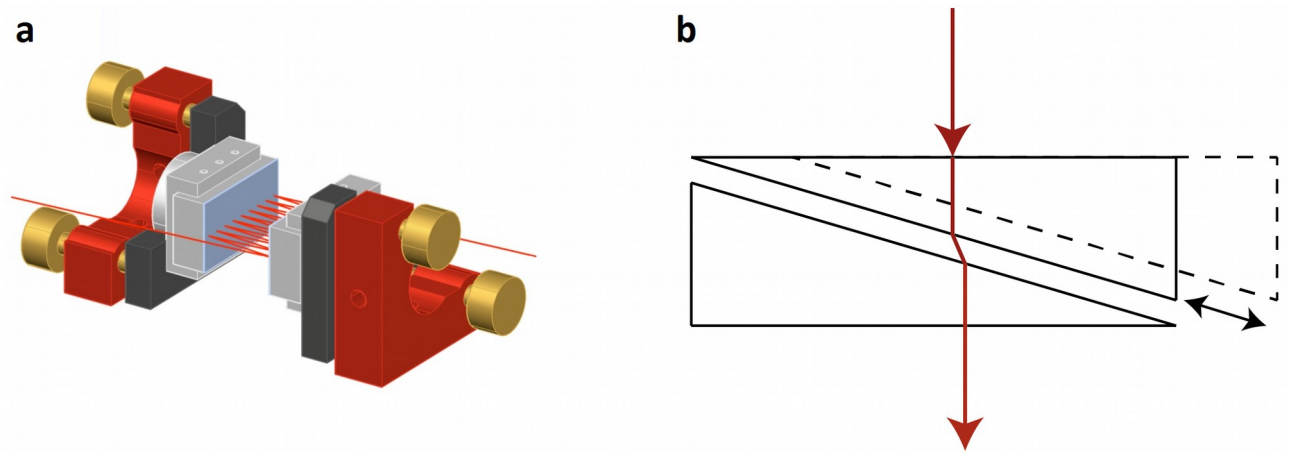

Figure S3. *a) Working mechanism of a couple of DCMs. Each reflection of the beam introduces negative chirping on a particular spectral region. b) Representation of a pair of wedges of variable thickness used to finely control the time delay between the two pumps without introducing deviation of the beam direction.*

The recorded signal is

$$\Delta A = log\left(\frac{I_{probe}^{on}}{I_{ref}^{on}}\frac{I_{ref}^{off}}{I_{probe}^{off}}\right) \qquad (1)$$

where I_{probe} is the light intensity arriving on the probe array in presence (^{on}) or absence (^{off}) of the pumps. By switching the time ordering between the two pumps, rephasing and non-rephasing maps are collected and Fourier Transform along their time delay yields the excitation frequency axes.

The collected signal consists in the interference between the emitted third order response of the sample E_s (that can be rephasing E_R or non rephasing E_{NR}) and the LO field E_{LO} . The intensity depends on the frequency ω_3 (dispersed by the monochromator) as well as on the time intervals τ_1 and τ_2:

$$I(\omega_3,\tau_1,\tau_2) = |E_{LO}(\omega_3)e^{i\omega_3\Delta\tau_{LO}} + E_S(\omega_3,\tau_1,\tau_2)|^2 =$$

$$|E_{LO}(\omega_3)|^2 + |E_S(\omega_3,\tau_1,\tau_2)|^2 + |E_{LO}(\omega_3)|e^{i\omega_3\Delta\tau_{LO}}E_S(\omega_3,\tau_1,\tau_2) \qquad (2)$$

where $\Delta\tau_{LO}$ is the E_3-E_{LO} delay. Two Fourier Transformations (FTs) are required to switch from τ_1 , τ_2 , τ_3 to ω_1 , τ_2 , ω_3, that represent the desired variables used to plot the final 2D spectrum. In our set-up the FT on τ_3 (yielding the dependence on the ω_3 frequency) is performed by the monochromator. The intensity term $|E_{LO}(\omega_3)|^2$ is subtracted from equation (1) by recording I_{probe}^{off} and normalized during each acquisition using the chopper technique.

The signal intensity $|E_s(\omega_3,\tau_1,\tau_2)|^2$ is very small (being a third order response) and can be neglected. The remaining intensity is proportional to the real part of the product $E_{LO}^{*}(\omega_3)e^{i\omega_3\Delta\tau_{LO}}E_S(\omega_3,\tau_1,\tau_2)$. It is indeed possible to show that the pure absorptive 2D spectrum is equal to the real part of the sum of Rephasing (R) and Non-Rephasing (NR) spectra [2], [5]:

$$S(\omega_1,\tau_2,\omega_3) = R\left\{\int_0^\infty d\tau_1 \int_0^\infty d\tau_3 [S_R(\tau_1,\tau_2,\tau_3)S_{NR}(\tau_1,\tau_2,\tau_3)]e^{-i\omega_1\tau_1}e^{-i\omega_3\tau_3}\right\} \qquad (3)$$

The phase term $e^{i\omega_3\Delta\tau_{LO}}$ can be subtracted by collecting the interference E3-E_{LO} separately. The procedure consists in making E3 and LO interfere through a pinhole in a cell filled up with the same solvent used to dissolve the dye for the 2D experiment, in order not to change the dispersion conditions of the beams. The FFT of the recorded interference spectrum is first cleaned from the zero time contribution and from the complex conjugate part by means of a suited designed Gaussian

filter. Then the signal is Inverse Fourier transformed (IFFT) back to the frequency domain, and the phase is recovered and fitted with a linear function $\alpha(\omega_3) = c \cdot \omega_3$ (see figure S4). The recorded signal is then multiplied by $e^{i\alpha\omega_3}$, so that the term $e^{i\omega_3 \Delta\tau_{LO}}$ is canceled.

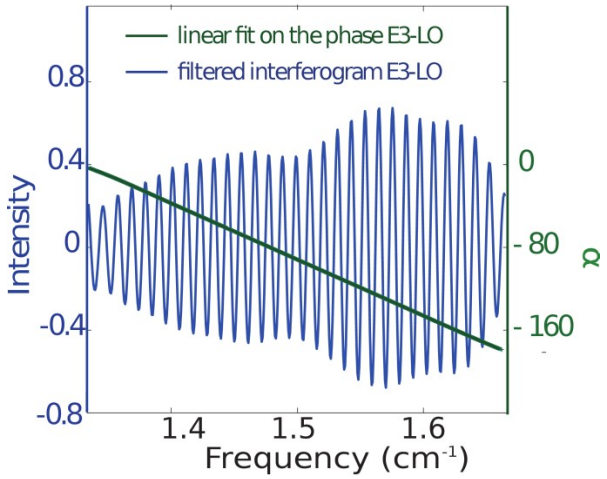

Figure S4. *Example of the recorded E3-E_{LO} interferogram after application of a Fourier filter (blue curve), on top of the linear fit on the E3-E_{LO} phase (green line).*

For each value of τ_2, a 2D map ω_3-τ_1 is recorded (R or NR). However, the third order Echo signal is superimposed to the pump probe between E3 and E_{LO}, with LO delayed by about 300 fs with respect to E3. Filtering out this contribution is straightforward by using a FT in ω_3 that allows separating the pump probe (at $\tau_3 = 0$) from the relevant signal, which occurs at $\tau_3 \neq 0$. Static contribution and noise are filtered out from the FT before going back to the inverse FT (IFT) that produces complex matrices for R and NR spectra. We can rewrite equation (2) as

$$S(\omega_1, \tau_2, \omega_3) = R[S_R(\omega_1, \tau_2, \omega_3) e^{-i\omega_3 \Delta\tau_{1,R}} + S_{NR}(\omega_1, \tau_2, \omega_3) e^{-i\omega_3 \Delta\tau_{1,NR}}] \quad (4)$$

The sign convention is such that for $\tau_1 < 0$ the scanned field E1 is delayed with respect to E2. In this region, as already mentioned, the interferograms R and NR must overlap because they are represented by the same diagram. If they do not exactly overlap, a constant calibration factor is used to correct the time step $\delta\tau_1$ of the fine delay generated by the wedges. Once the absorptive 2D spectra is calculated, some optimization procedures are required, based on two assumption:

1. The Projection Slice theorem states that the projection of the absorptive map on the ω_3 axis should coincide with the pump probe spectrum at the same τ_2 and in the same experimental conditions [5], [6]. In order to satisfy this theorem, we need to minimize the χ^2 function

$$\chi_{\dot{c}} = \sum_{\omega_3} \{[S_{PP}(\omega_3, \tau_2) - \int S(\omega_1, \tau_2, \omega_3)]^2\} \quad (5)$$

The peak position should not be altered by the phase [6], [7]. This mathematically translates in two conditions of minimization of the following χ 2 functions, both for R and NR signals:

$$I(\omega_3, \tau_1, \tau_2) = \left|E_{LO}(\omega_3) e^{i\omega_3 \Delta\tau_{LO}} + E_S(\omega_3, \tau_1, \tau_2)\right|^2 = \left|E_{LO}(\omega_3)\right|^2 + \left|E_S(\omega_3, \tau_1, \tau_2)\right|^2 + \left|E_{LO}(\omega_3)\right| e^{i\omega_3 \Delta\tau_{LO}} E_S(\omega_3, \tau_1, \tau_2) \quad (6)$$

Figure S5 shows an example of the projections of an experimental 2D spectrum onto the axis ω_3 and ω_1, superimposed to the pump-probe spectrum and to the $S_{R/NR}$ projection onto ω_1, respectively. In order to satisfy the two conditions listed above, the curves must be as close as possible. The above criteria are used to find the best values of two key parameters. First, the exact zero of τ_1: in fact, the wedges position for which τ_1=0 can be slightly different from the one estimated in the wedges calibration procedure (described in ref. [8]). Second, the estimated value of α from the linear fitting procedure described above can be ambiguous due to possible change in the experimental conditions during the E3-LO interference measurement. A minimization cycle is performed by varying both these parameters in order to minimize equations (5) and (6).

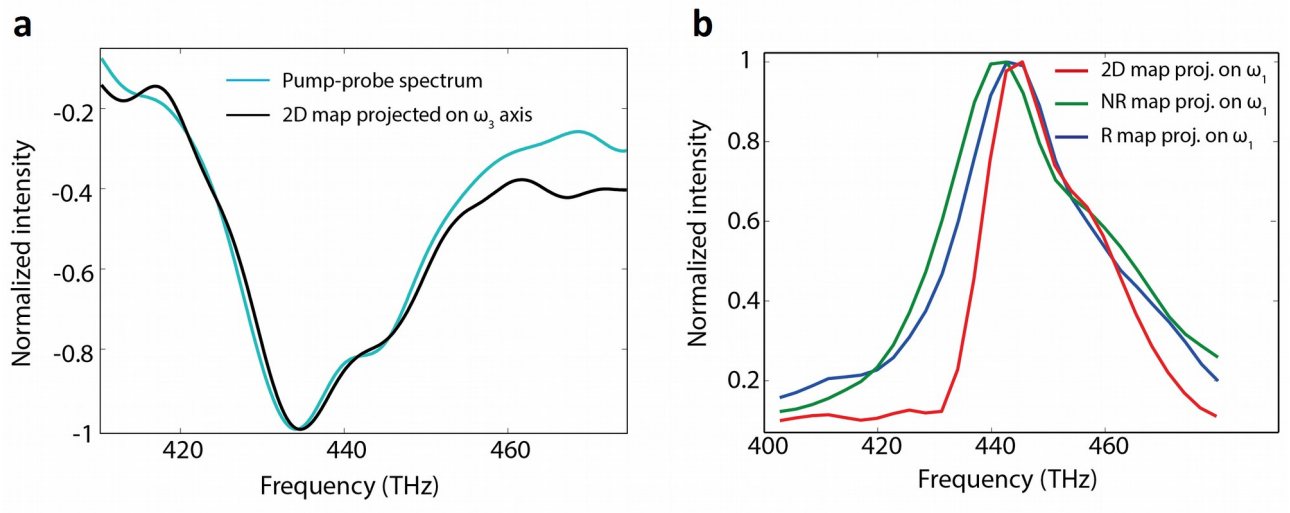

Figure S5. *a) Example of pump probe spectrum overlapped with the absorptive 2D spectrum projected on the ω_3 axis. b) Example of condition 2: R_1, R_2 and Echo maps projected on ω_1 axis.*

Solvatochromism of monomer and aggregate

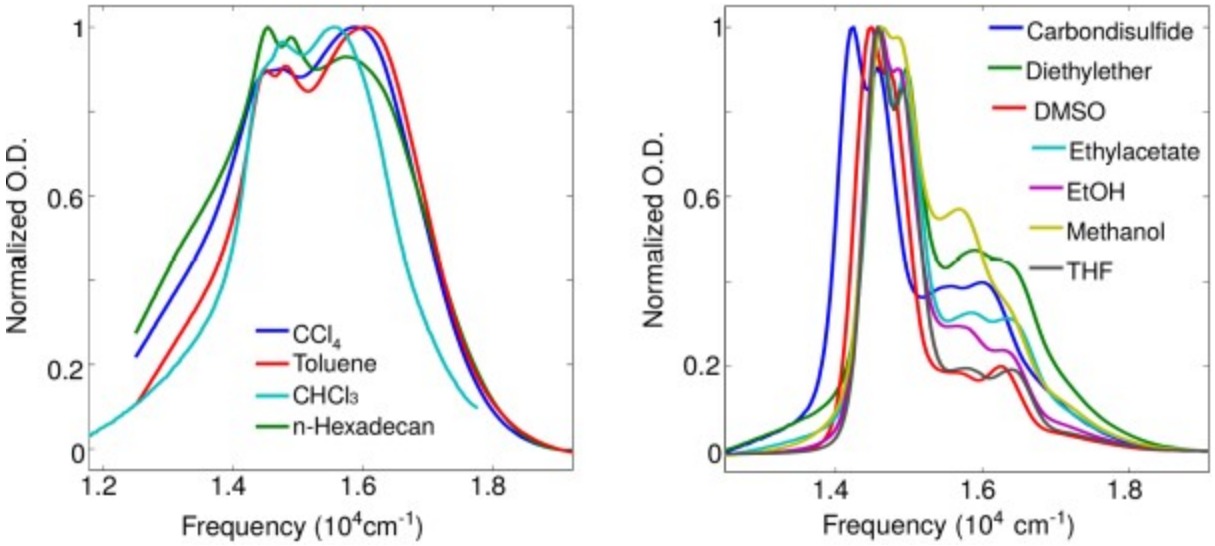

Figure S6. *Linear absorption spectra of the Zn(II)-Phtalocyanine dye in solvents that prevent aggregation (a) and in solvents that favor aggregation (b). The different intensity ratio between aggregate and monomer absorption bands is due to different amount and/or aggregate size.*

The monomer absorption spectra show appreciable solvatochromism (Fig. S6). A first analysis in this respect involved only those solvents where aggregation effects are sufficiently small. The

suitable solvents include non-polar CS_2, weakly polar diethyl ether (DEE), ethyl acetate and THF, polar DMSO and hydrogen-bonding ethanol and methanol. Experimental data for the lowest transition are shown in Fig. S7. A distinct behavior separates nonpolar, polar, and protic solvents. The most striking feature here is the large red-shift (> 300 cm^{-1}) passing rom DEE to CS_2, which indicates a large dispersive behavior of the solvatochromism.

In order to reproduce the experimental spectra monomers were optimized in vacuum at the B3LYP/6-31G* level. Excited state calculations were performed with PCM solvent at the M062X/6-31+G* level. Test calculations with other functionals or larger basis sets gave qualitatively similar results. For the polar solvents series, the first band red-shifts with increasing polarity, in agreement with the π–$\pi*$ character of the electronic transition. We calculated the first two vertical excitation energies of ZnPc in various solvents, excluding the protic ones. The calculations were performed on in vacuum optimized structures. The results, shown in Fig. S7, indicate that the calculations are able to reproduce the large red shift between DEE and CS_2. Conversely, the red shift observed in DMSO is not reproduced by the calculations.

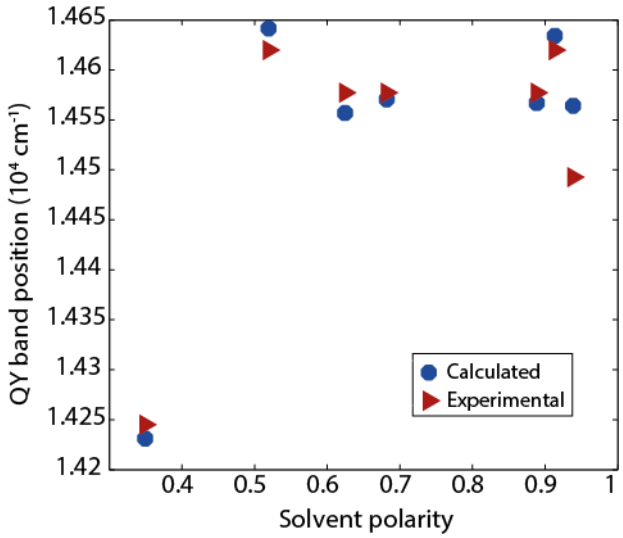

Figure S7. *Experimental (red triangles) and calculated (blue dots) excitation energies of ZnPc dye in different solvents. The x-axis is the solvent polarity* $\frac{\varepsilon-1}{\varepsilon+2}$.

TEM characterization of aggregates

Fig. S8 reports the TEM image of the sample in chloroform (where aggregation occurs), showing a typical shape of the molecular superstructures in this medium. The dark parts result from the contrast of the zinc central atom in the molecule macro-structure. Even if the overall aggregate is mostly disordered, a small degree of order is visible in some portion of the image, showing the monomer packing along preferred directions and forming fibrous structures.

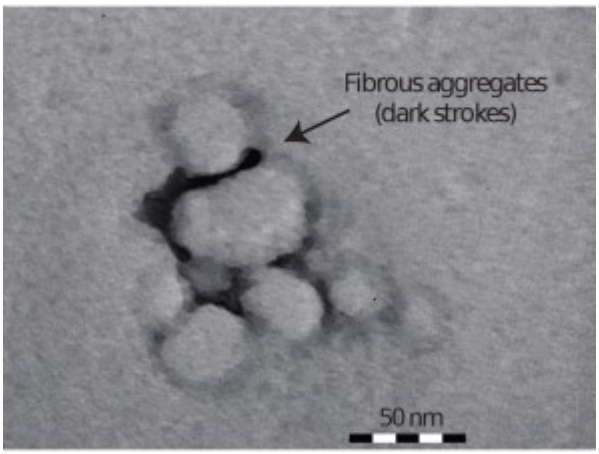

Figure S8. *TEM image showing the presence of branched aggregates.*

Deconvolution analysis of the linear absorption spectra

The deconvolution of the linear absorption spectra of the dye in ethanol and chloroform has been carried out in order to identify the monomer contribution to the whole absorption in presence of aggregates. The collected spectra and the fitting functions are shown in Fig. S9.

The analysis consist in a two-step procedure: first we fitted the monomer absorption in ethanol with five Gaussian features (panel a, Fig. S9). These five functions plus three more Gaussian features are then used to fit the spectrum in chloroform, where aggregation occurs (panel b of Fig. S9). The parameters (FWHM, center frequency and height ratio) of the five Gaussian functions used to fit the monomer contribution where kept fixed in order to reproduce exactly the monomer lineshape, except for a small frequency shift, necessary to take into account the difference in solvents between the spectra in panel a and b. The sum of monomer fitting functions is shown in red in FigS9b. The

three green features are the Gaussian function referred to the aggregate signal.

We computed the ratio between area under the red curve and the total fitted area (black curve), obtaining a monomer contribution of 26% to the whole absorption spectrum. In addition, we estimated the contribution of the vibronic bands to the aggregate band. This was accomplished by calculating the ratio between the area under the three Gaussian functions used to fit the vibronic band of the monomer in chloroform (centered at around 15530 cm^{-1}, 16420 cm^{-1} and 17390 cm^{-1}) and the area under the fitted aggregate band (green curves).

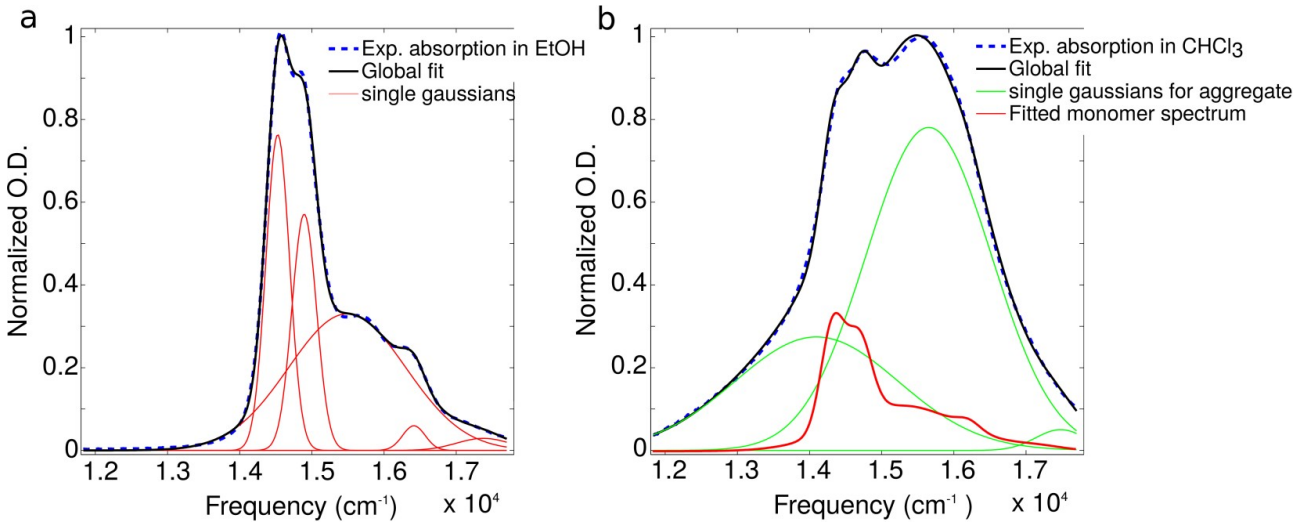

Figure S9. *Deconvolution analysis of the linear absorption spectra. a) Experimental absorption of the monomer in ethanol (dashed blue line) plotted on top of the total fitting function (black line), obtained by summing 5 Gaussians features (red curves). b) Experimental linear absorption of the dye in chloroform (dashed blue line), plotted on top of the total fitting function (black line), obtained by summing 5 Gaussian features reproducing the monomer absorption (sum in red), plus three Gaussian used to fit the residual aggregate bands.*

Broadband pump-probe of the monomer in Diethyl Ether

Pump probe data and the respective global analysis for measurements performed on ZnPc in diethyl ether are shown in Fig. S10. Similarly to the results obtained in ethanol solution, the ground state

bleaching recovery can be fitted by using three-exponential functions. The long time-component is kept fixed to the value of 4 ns, in agreement with reference [9]. The EADS corresponding to the three spectral components with increasing lifetimes have similar lineshape, except for a slight change in the intensity ratio between the two Q-states bleaching at increasing lifetime. The calculated time-constants are of the same order of magnitude than in ethanol, suggesting that the electronic properties of the monomer are only slightly influenced by solvents effect.

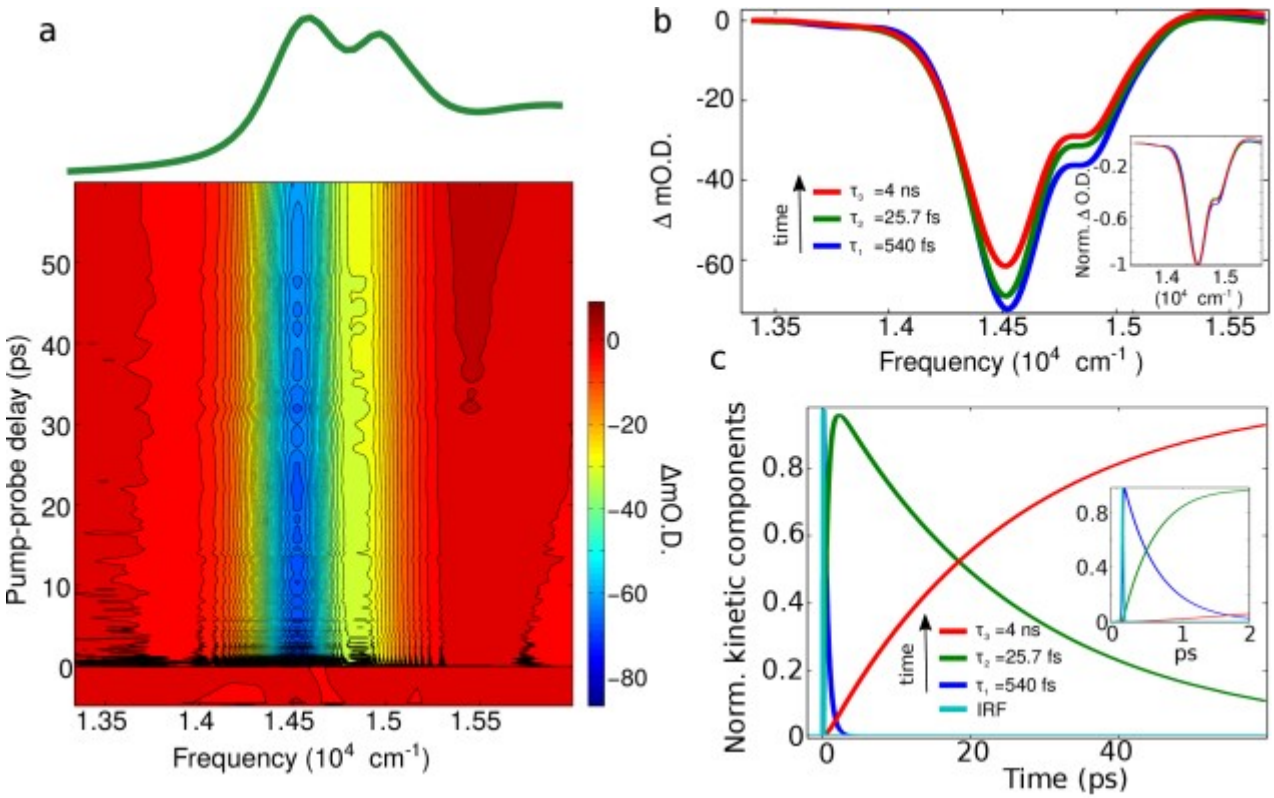

Figure S10. *a) Broadband pump-probe 2D time-frequency map of the dye in diethyl ether, where only the monomer is present (linear absorption spectrum on top). b) EADS retrieved from Global analysis using a sequential model involving three kinetic parameters. Normalized EADS in the inset. c) Normalized kinetic components describing the time-evolution of the EADS. Zoom of the first 2 ps in the inset.*

Broadband pump-probe at initial timescale recorded in ethanol, diethylether and chloroform

The initial time-gated pump-probe spectra of the dye in the three solvents are reported in Fig. S11.

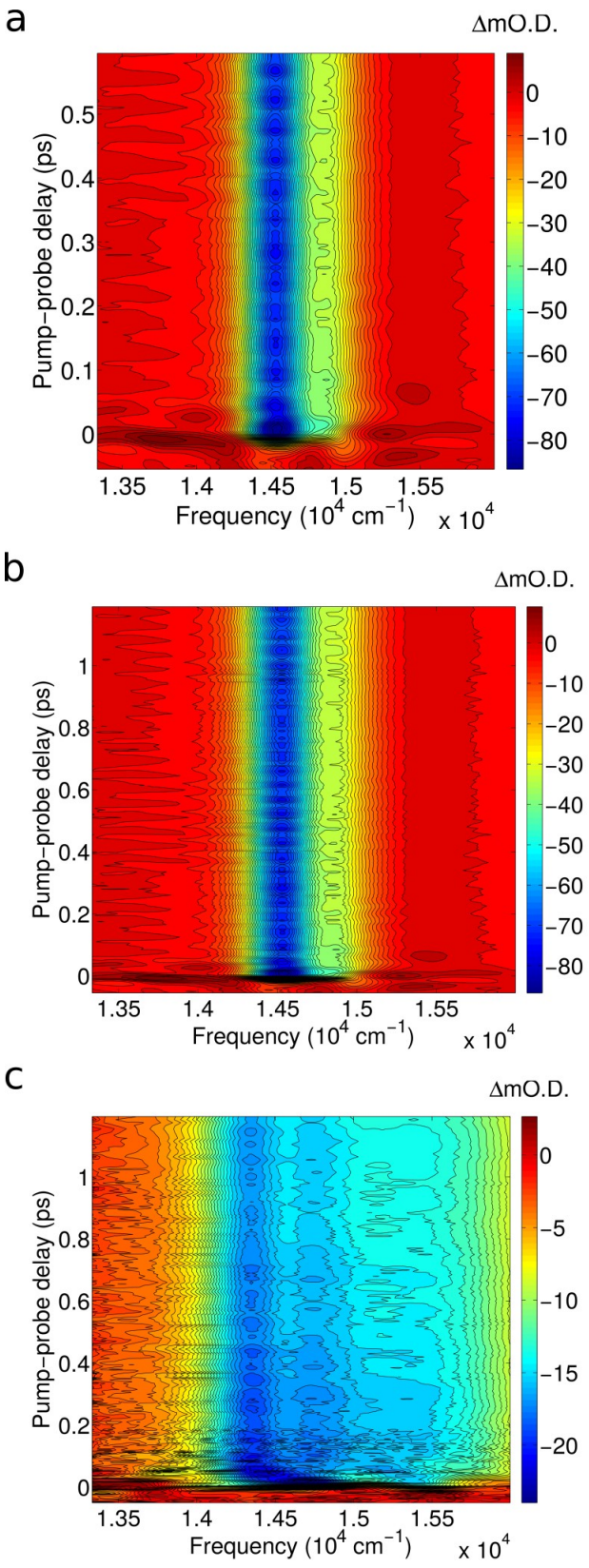

Figure S11. *Pump-probe data at short timescales collected in ethanol (a), diethyl ether (b) and chloroform (c).*

Observation of temporal oscillation in Pump-probe signal

On short timescale (less than 1 ps) we observed oscillations in the kinetic traces corresponding to the maximum of the GSB signal, both in ethanol and in diethyl ether solution. The lower panel of Fig. S11 a) and b) presents single-frequency kinetic traces extracted from the map in Figure 2a (of the main text) and S10a respectively, for the two solvents. Fourier-transform analysis extracts two main oscillation frequencies at 730 cm^{-1} and 760 cm^{-1}, which are consistent with Raman vibrational modes reported in ref. [10]. We carried out pump-probe measurements on the pure solvent to rule out the possibility that the oscillation were due to solvent.

We estimated the error on the observed oscillations from the maximum fluctuation of the baseline before zero time-delay. The error amplitude resulted to be 0.04 mO.D., which is very small compared to the oscillations amplitude, ranging from 3 to 5 mO.D.

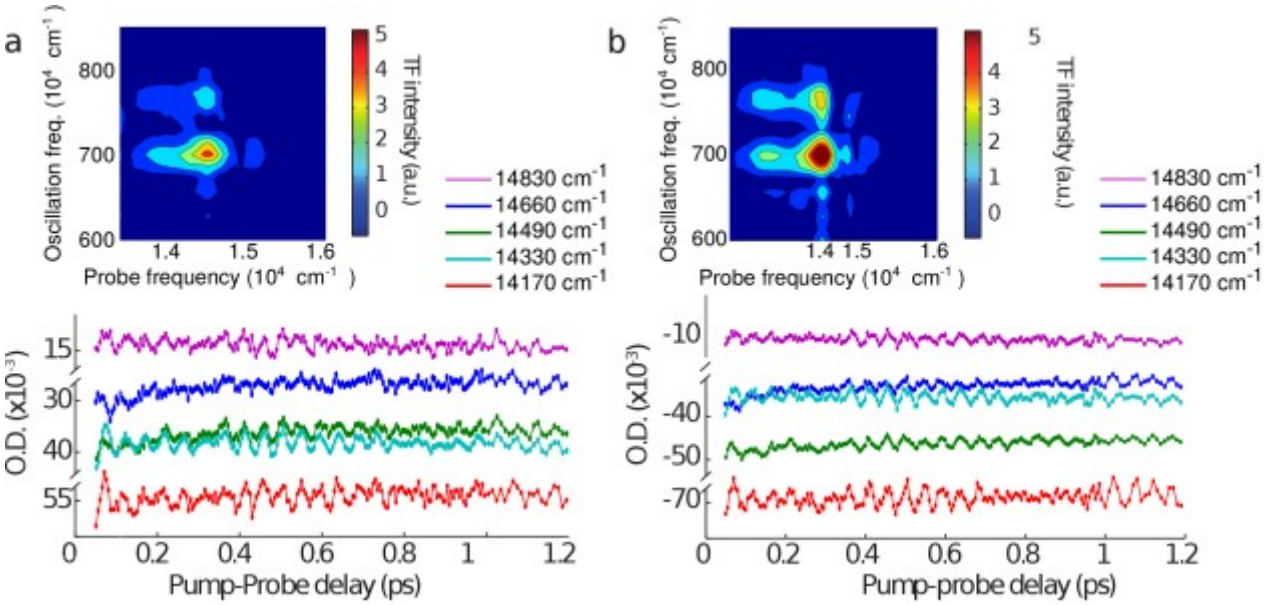

Figure S12. *Decay kinetics at different frequencies and short timescale from the 2D pump-probe measurements in ethanol (a) and in diethyl ether (b) solution, showing oscillatory behavior at around 730 cm^{-1} and 760 cm^{-1} (Fourier transform map in the inset).*

2DES of the monomer in Ethanol

The 2DES maps recorded as a function of population time τ_2 in ethanol are reported in Fig. S13. Spectral diffusion is clearly visible by the antidiagonal broadening of the bleaching lineshape.

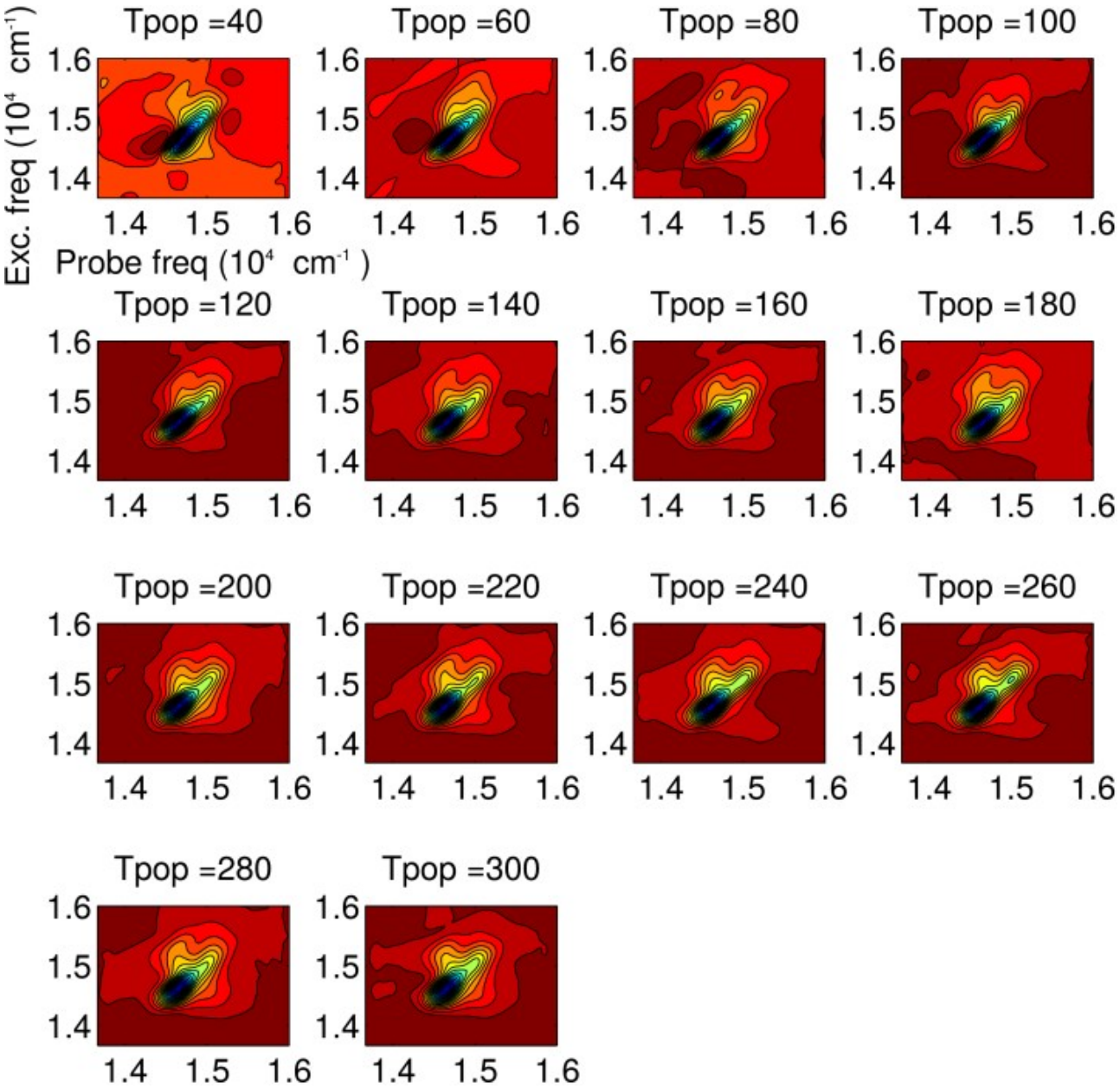

Figure S13. *Absorptive 2DES maps of the dye in EtOH at recorded at different τ_2 between 40 and 300 fs. The antidiagonal broadening of the ground state bleaching component over time is indicative of spectral diffusion occurring on those timescales.*

To compute the ellipticity as specified in eq. 1 of main text, we estimate FWHM of diagonal and antidiagonal lineshape from the maps in Fig. S13. As reported in the main text, the antidiagonal cut used to compute homogeneous lineshape is taken at a frequency corresponding to the low-energy Q-state of the monomer 14580 cm^{-1} thus avoiding the broadening due to overlap with cross-peaks. In Fig. S14 we show two antidiagonal slices taken at different frequencies: the red line at 14800 cm^{-}

[1] is a convolution of diagonal and off-diagonal contributions; the blue line at 14580 cm^{-1} consists only in the diagonal contribution, thus resulting much narrower (see also fig 4b of main text).

The diagonal lineshape, resulting in inhomogeneous broadening, is the convolution of the two Q-bands contribution. The FWHM is calculated by deconvolving the two components into two Gaussian functions, as reported in Fig. S15 in case of a selected τ_2 of 140 fs.

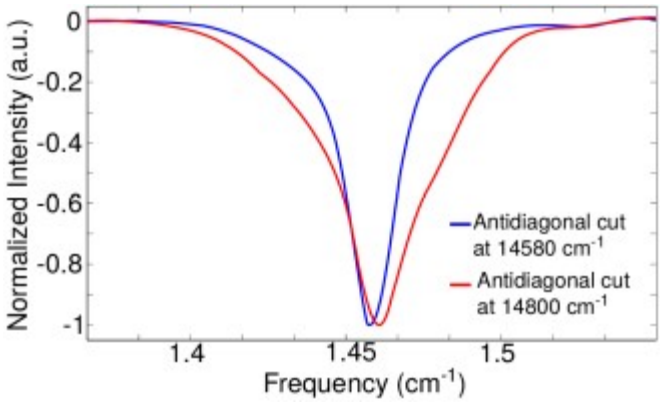

Figure S14. *Antidiagonal (b) lineshape extracted from 2DES maps at different frequencies. The spectra at 14800 cm^{-1} (red line) is clearly broadened due to overlap with cross-peaks. To calculate the ellipticity we choose the cut at 14580 cm^{-1} (blue line), where the overlap with cross-peaks is negligible.*

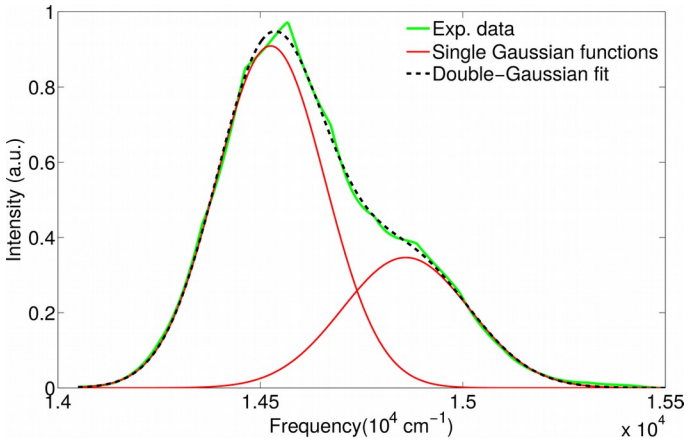

Figure S15. *Green line: diagonal lineshape from 2D spectra at τ_2 = 140 fs. Red lines: single Gaussian components representing low energy and high energy Q-state contributions. Dashed black line: total fitting function (sum of the two Gaussian functions).*

2DES of the monomer in Diethyl Ether

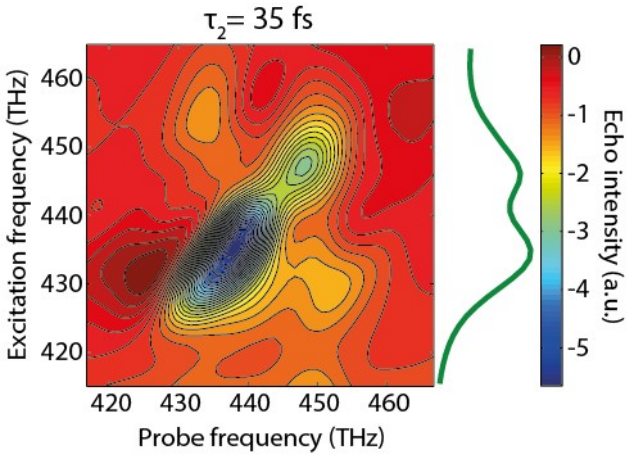

Figure S16. *2DES maps recorded at τ_2 = 35 fs of the dye in diethyl ether. The cross peaks attributed to the Q-states coupling are well defined on both the high frequency and low frequency side of the 2D spectra, as well as the two Q-states components on the diagonal slice. Linear absorption spectra of the dye in diethylether is shown on the right side of the map.*

Deconvolution analysis of the Pump-probe data in chloroform

We estimated the residual bleaching signal of the monomer in chloroform by deconvolving the three EADS obtained from Global analysis performed on the pump-probe data (see Fig. 5 of main text). The deconvolution analysis is reported in Fig. S17. We fitted the three EADS with a convolution of different Gaussian features. The contribution of the residual signal of the monomer with respect to the initial species has been estimated by computing the ratio between the sum of the areas area under the curves used to fit the first EADS and the sum of the areas under of the curves used to fit the third EADS (which we assume to be assigned only to monomers, since on the long timescale the aggregate bleaching is completely recovered). We found that the ratio is 24% of the initial signal. This result is in agreement with the calculated monomer contribution to the linear spectra, obtained by deconvolution of the linear absorption data, reported above (Fig. S9).

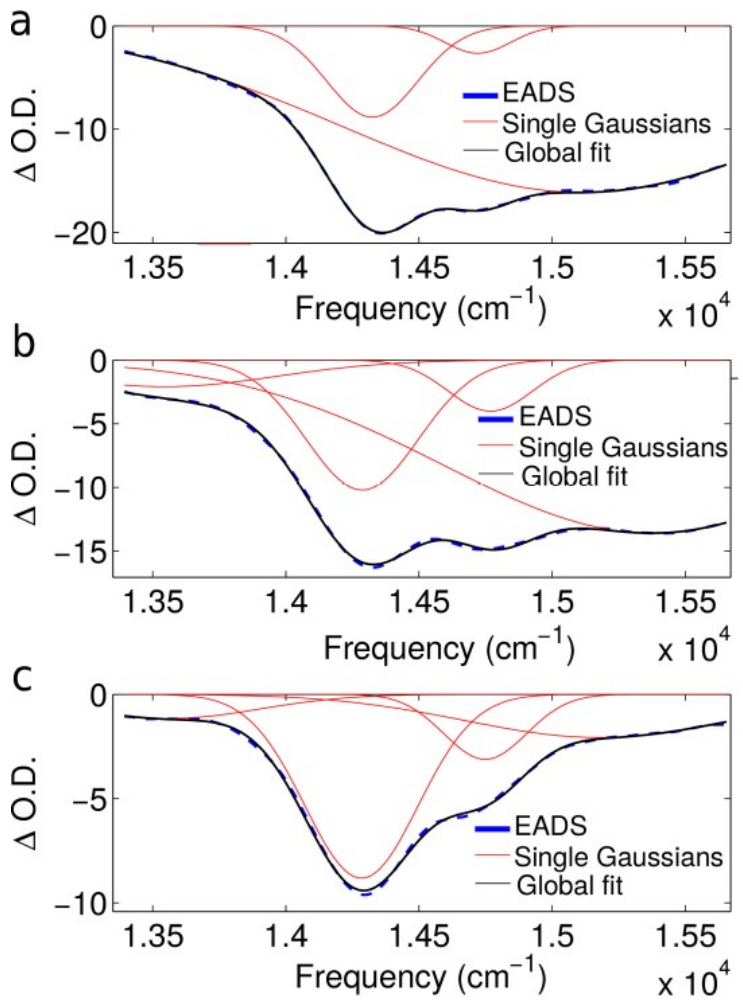

Figure S17. *Deconvolution analysis of the EADS obtained by Global analysis of the pump-probe data collected in chloroform. Blue lines are the EADS components at short (a), intermediate (b) and long timescale (c). Red curves are the single Gaussian fitting features and black curves are the sum of the fitting functions.*

2DES of the system in chloroform

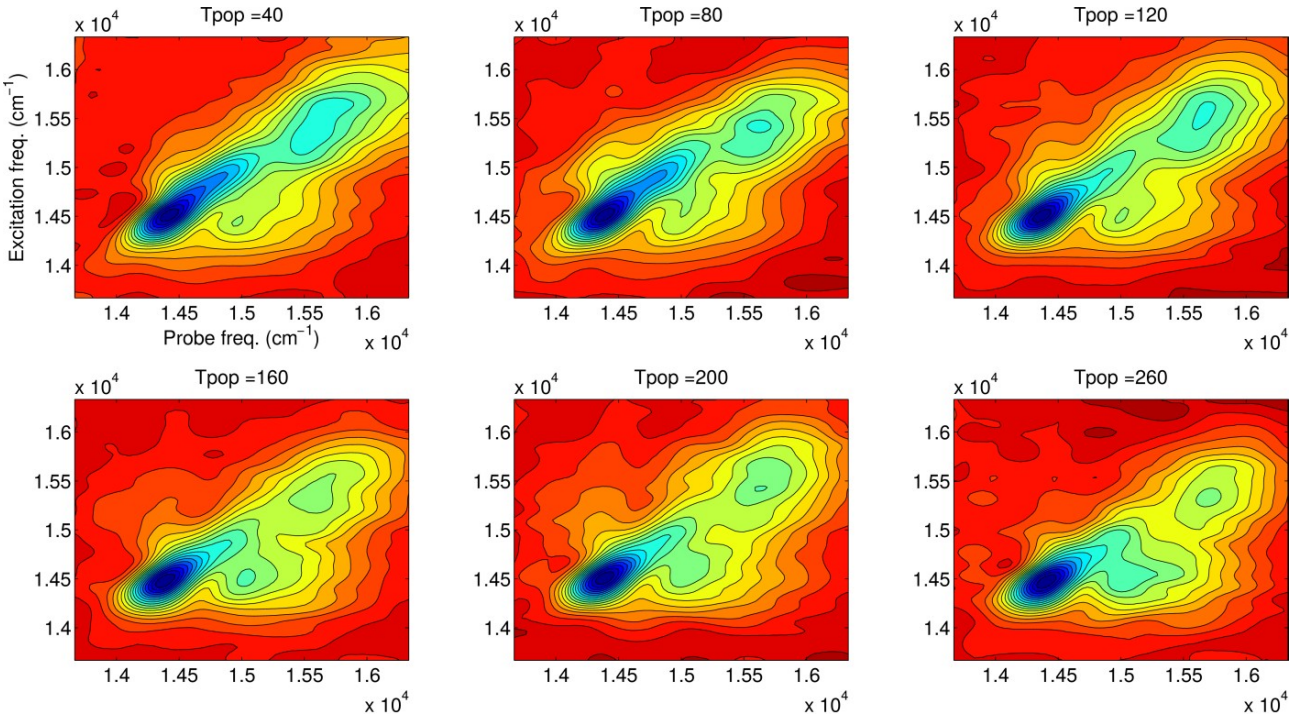

Figure S18. *Absorptive 2DES maps of the dye in Chloroform in condition of low H-band intensity recorded at different* τ_2 *between 40 and 260 fs.*

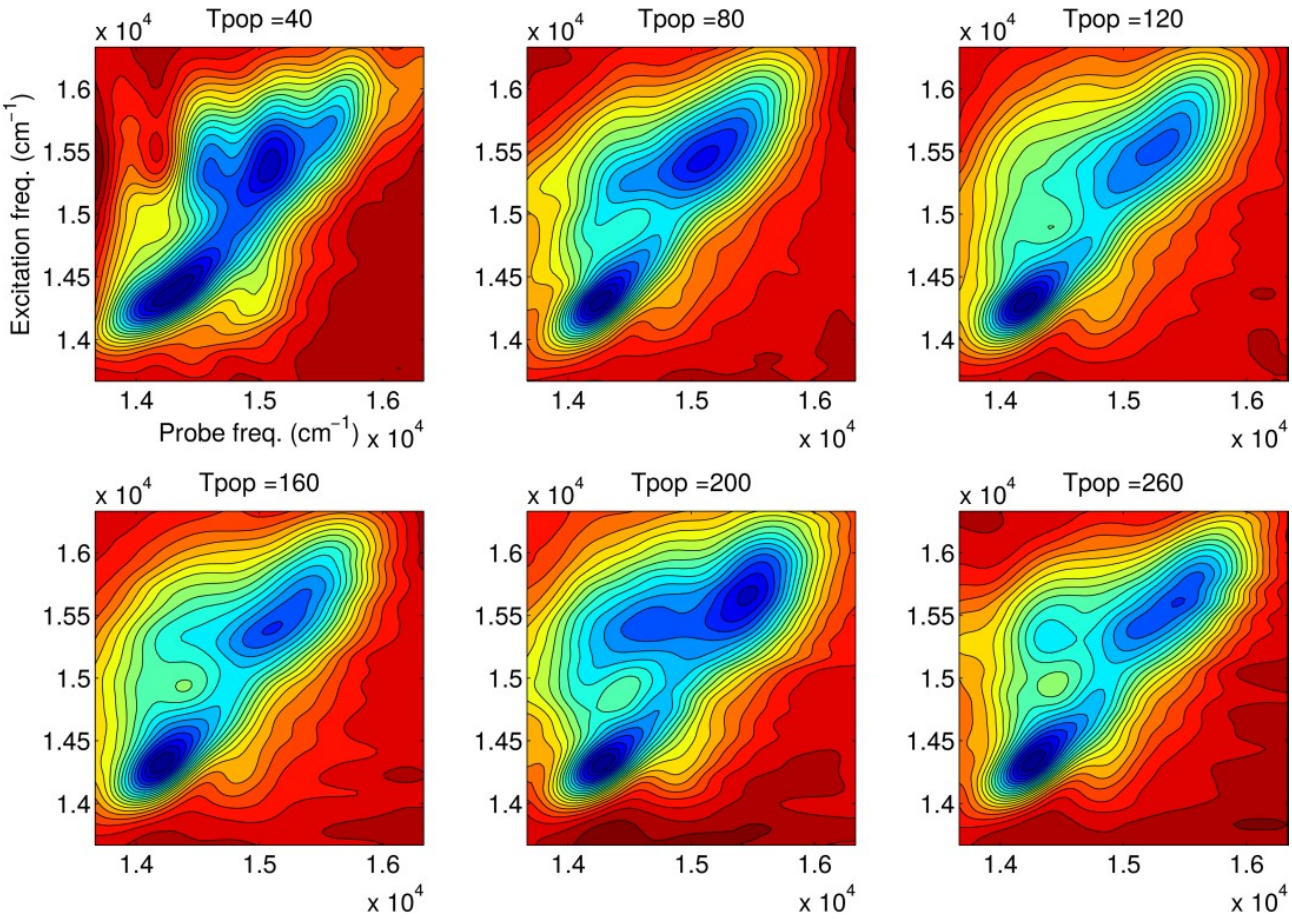

Figure S19. *Absorptive 2DES maps of the dye in Chloroform in condition of high H-band intensity recorded at different* τ_2 *between 40 and 260 fs.*

Quantum chemical calculations

Calculations at the DFT level were carried out in order to optimize the geometry of a simple dimeric system and to compute the electronic couplings. Results of quantum chemical calculations, in terms of dipole arrangements and transition dipole moments, were then used to build up an extended aggregate model based on a Frenkel Hamiltonian describing the delocalized exciton state.

After the optimization of several dimer models, we identified two most stable configurations, which differ in energy by less than 0.1 kcal/mol. The geometries of the two dimers are shown in Fig. S20a. From the interactions between the Q-states of the two molecules forming the dimer, four electronic levels arise in the dimeric system, whose energies and calculated transition dipoles are reported in Tab. ST2. Tab. ST1 shows the same parameters in case of the monomer. The electronic couplings between the states of different monomers in the two dimers are reported in Tab. ST3. Only the two upper electronic transitions are allowed, producing the observed blue-shift in the absorption spectra.

The two dark states below the monomer S_1 state act as energy traps, introducing non-radiative pathways that slow down the ground state recovery and reduce the fluorescence QY efficiency of the dye.

Monomer

State	Energy (cm^{-1})	μ^2 ($debye^2$)
Q_y	14463	15.296
Q_x	15087	11.261

Table ST1. *Energies of the electronic levels and calculated values of the transition dipole moments or the monomer in methanol.*

Dimer 1			***Dimer 2***	
State	*Energy (cm^{-1})*	*μ^2 ($debye^2$)*	*Energy (cm^{-1})*	*μ^2 ($debye^2$)*
1	13844	0.1379	13979	0.2162
2	14525	0.0896	14646	0.8479
3	15313	27.7888	15421	29.0639
4	15856	24.4542	15721	21.3346

Table ST2. *Energies of the electronic levels and calculated values of the transition dipole moments for the optimized structures of the dimers.*

For each dimer, we computed the exciton couplings among the Q states of the different monomers, which are reported in Tab. T2. The couplings involving similarly polarized transitions are larger than those involving orthogonal transitions, although the latter are not at all negligible. In Dimer 2, the couplings are generally lower than in Dimer 1, and a negative cross-coupling appears between the Qy state of one ZnPc and the Qx state of the other monomer.

Coupling	*Dimer 1*	*Dimer 2*
Qy-Qy	732 cm^{-1}	646 cm^{-1}
Qy-Qx	80 cm^{-1}	149 cm^{-1}
Qx-Qy	128 cm^{-1}	- 412 cm^{-1}
Qx-Qx	660 cm^{-1}	- 455 cm^{-1}

Tab. ST3 *Electronic couplings (cm^{-1}) computed on the two dimers. Qy is the lowest of the two Q states.*

In order to compare our results with the experiments, we computed the excitonic states of each dimer, their energies, and their dipole strength. In both dimers, the dipole strength is almost completely distributed in the two highest-lying states, in agreement with the H-character of the dimers. In particular, the highest energy state of Dimer 1(2) lies 1300(1200) cm^{-1} above the Qy state of the isolated monomer. As a comparison, the aggregate band in Chloroform peaks around 15560 cm^{-1}, ∼1100 cm^{-1} above the shoulder in the red side of the spectrum (see Fig. 1b) due to the monomer Qy band. To complete this analysis, we computed the spectra for the monomer and the dimers in two solvents favoring aggregation ($CHCl_3$ and CCl_4), assuming Gaussian line shapes (FWHM = 1000cm^{-1}). These spectra were superimposed to the experimental spectra of ZnPc in $CHCl_3$ and CCl_4 (see Fig. 9b). This comparison suggests that aggregates formed in CCl_4 are more extended than those in $CHCl_3$, which are well described by a dimeric model.

Extended aggregate model

The calculations reproduce the experimental blueshift of the aggregate respect to the monomer absorption spectra, but do not provide physically meaningful pieces of information concerning the line-shape in the aggregate and the degree of electronic delocalization. To understand the effect of dye-aggregation on the electronic properties of the system, it is necessary to take into account long range couplings among the monomers. In addition, static and dynamic disorder must be included, especially when the intermolecular interactions are weak compared to the bath fluctuations. To describe the spectral properties of the system and to disentangle the contributions of the different factors affecting the lineshape, we developed a structural model based on a Frenkel Hamiltonian

that describes the delocalized excited state of the aggregate following reference [12].

In order to describe an aggregate containing 2000 molecules, a Frenkel Hamiltonian of 2000 sites was constructed, where the diagonal elements ε_{mm} are the monomer transition energies which have an inhomogeneous distribution due to the static disorder. The off-diagonal coupling elements Vnm in the extended dipole approximation [13]–[15] were calculated starting from the geometry parameters and the charges magnitudes of the optimized dimers. In our model, each monomer is formed by two perpendicular extended dipoles μ (for the two transitions Qy and Qx) with point charges qy= ± 0.52e and qx= ± 0.45e (being e the electron charge) and length l=3.98 Å (same for both). The distance between two adjacent dipoles is r = 4.59 Å. We build up a linear aggregate model by stacking one molecule on top of the other such that the dipoles are relatively oriented either as Dimer 1 or Dimer 2 (random choice). The total number of dimers is 1000.

The static disorder is introduced as a Gaussian distribution in the random diagonal elements offsets, while the dynamic disorder is included using Lorentzian homogeneous lineshapes of various widths. The best fit of the experimental lineshape, represented by the simulated spectra in Fig. 9d, is achieved using a homogeneous linewidth of 1400 cm^{-1} and inhomogeneous distribution of 400 cm^{-1} (see Fig. S15). Using these parameters we closely reproduce the experimental absorption spectrum in the presence of large aggregates concentration, as shown in Fig. S20d.

Such approach represent a big advance in understanding how strong the homogeneous and inhomogeneous contributions affect lineshapes. A homogeneous contribution of 1400 cm^{-1} corresponds to a dephasing process occurring in tens of fs. The amount of inhomogeneous distribution, 400 cm^{-1}, is a large fraction of the coupling constant, thus evidencing a strong contribution due to orientational disorder and distance distribution among monomers.

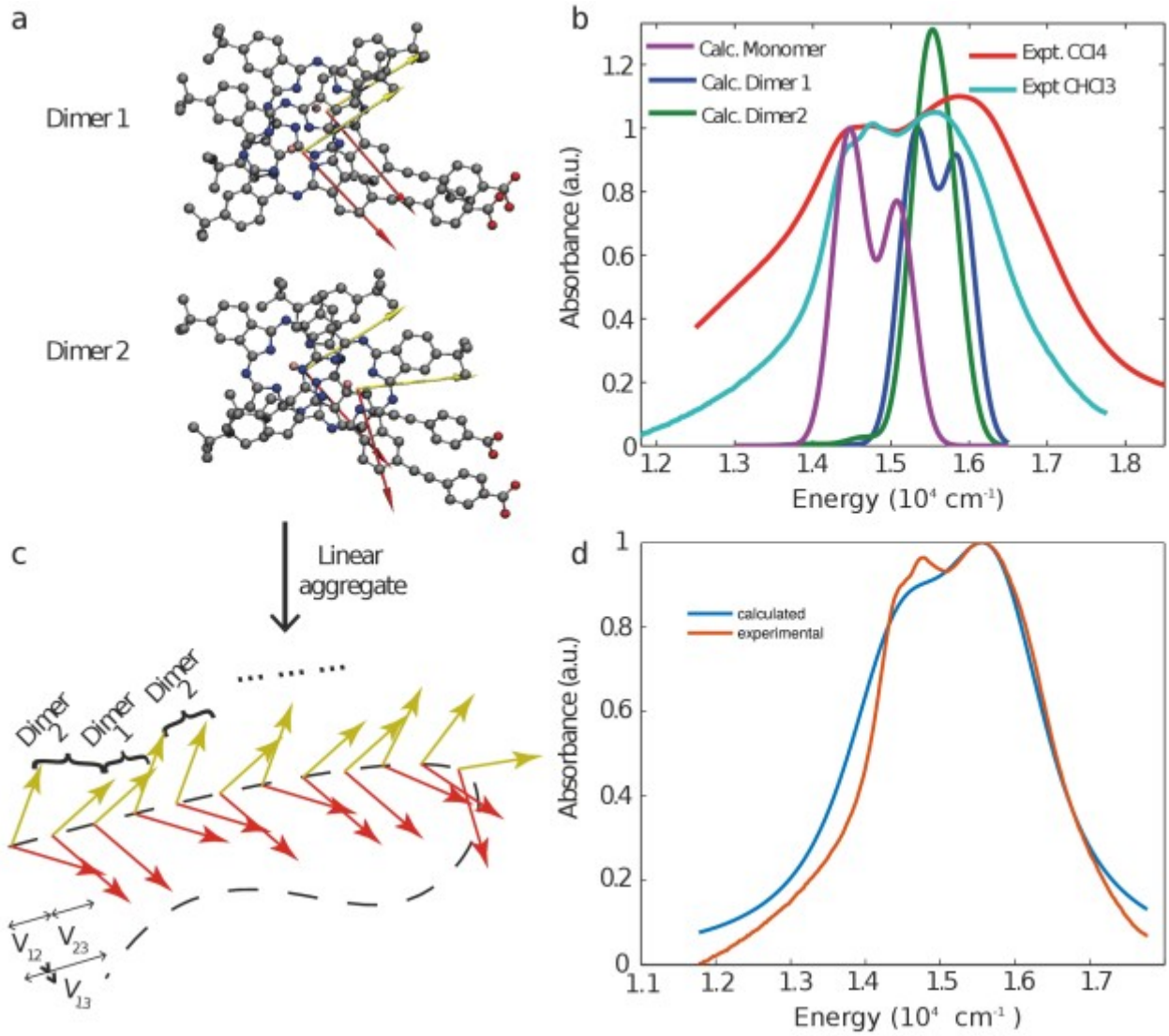

Fig. S20. *a) Optimized structures of the two most stable dimer structures. Transition electric dipole moments of the Q states are represented by red and yellow arrows for the first and the second states respectively. b) Calculated spectra for the monomer and Dimers 1 and 2, superimposed to the experimental absorption spectra in $CHCl_3$ and CCl_4. All the calculated spectra have been shifted by –1500 cm^{-1} to match the Qy band position. c) Scheme of the linear aggregate described by the Frenkel Hamiltonian: the relative orientation of two adjacent dipoles is chosen randomly between the Dimer 1 or Dimer 2 optimized structures. The couplings elements Vnm are calculated between adjacent Qx-Qx or Qy-Qy transition dipoles in the extended dipole approximation. d) Simulated spectra of the linear aggregate obtained from the diagonalization of the Frenkel Hamiltonian, on top of the experimental absorption spectra of the dye in $CHCl_3$.*

The possibility of introducing separately inhomogeneous and inhomogeneous broadening in our Frenkel model allows us to discriminate between static and dynamic disorder, and to modulate the lineshape, as shown in Fig. S21.

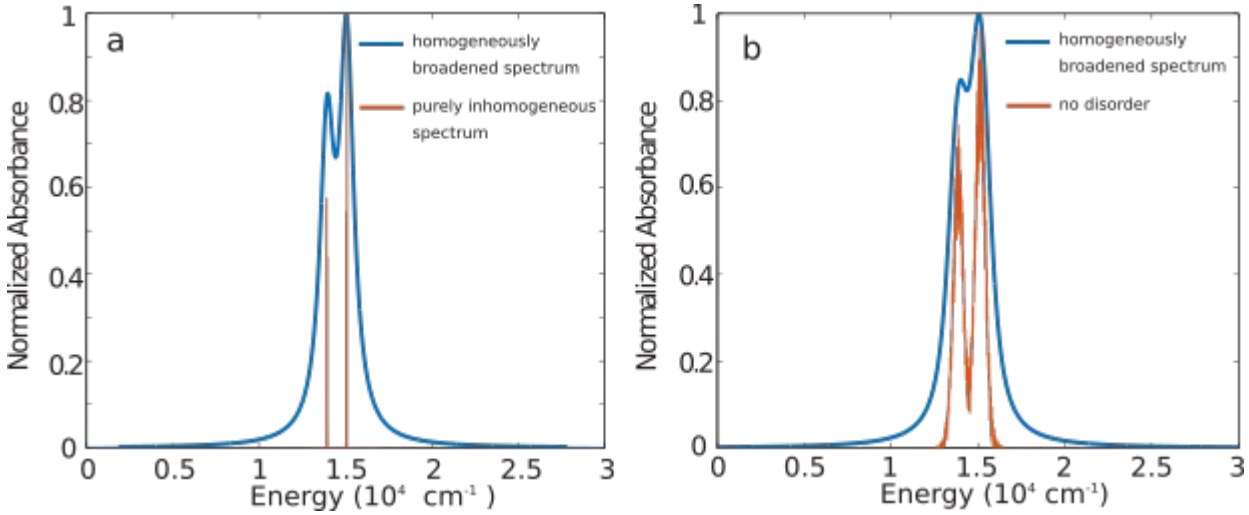

Figure S21. *Intermediate steps of the exciton spectral modeling. a) Simulated spectral components of the aggregate in absence of disorder and in case of a homogeneously broadened spectrum. b) Simulated spectral components of the aggregate in presence of only inhomogeneous disorder (400 cm^{-1} Gaussian width) and after adding homogeneous broadening (1400 cm^{-1} Lorentzian width). The preponderance of homogeneous broadening is a further confirmation that the system is partially ordered.*

To estimate the spatial extent of the exciton, i.e. the number of molecules participating in the excited state, we can look at the Inverse Participation Ratio (IPR), which is defined as $\frac{1}{\sum_{i=1}^{N} P_i^2}$, where P_i is the probability of the exciton being on site i (so the wave function at that site squared) [11]. This number will range from *0* to *N*, where *N* is the total number of molecules in the aggregate and corresponds to the number of molecules the exciton is delocalized over. In the present case, since each molecule contains two electronic states the IPR will range from 2 to 2N. Since we are interested in how many molecules the exciton is delocalized over, we will divide these number by 2 to account for this. Our computation shows the average exciton is delocalized over 3.6 molecules. When weighted by oscillator strength, the average exciton is delocalized over 5.9 molecules.

References

[1] G. Cerullo and S. De Silvestri, *Rev. Sci. Instrum.*, 2003, **74**, 1, 1–18.

[2] J. D. Hybl, A. W. Albrecht, S. M. Gallagher Faeder, and D. M. Jonas, *Chem. Phys. Lett.*, 1998, **297**, 3-4, 307–313.

[3] G. Cerullo, M. Nisoli, and S. De Silvestri, *Tech. Dig. Summ. Pap. Present. Conf. Lasers Electro-Optics. Conf. Ed. 1998 Tech. Dig. Ser. Vol.6 (IEEE Cat. No.98CH36178)*, 1997, **3616**, 70–73.

[4] N. Azzaroli, “Optical set-up development and software interface of 2D-Visible coherent spectroscopy experiment to investigate dynamics of multi-chromophoric molecular complexes” University of Florence, Italy, 2015.

[5] M. Khalil, N. Demirdöven, and A. Tokmakoff, *Phys. Rev. Lett.*, 2003, **90**, 4, 47401.

[6] J. D. Hybl, A. A. Ferro, and D. M. Jonas, *J. Chem. Phys.*, 2001, **115**, 14, 6606-6622.

[7] J. M. Anna, M. J. Nee, C. R. Baiz, R. McCanne, and K. J. Kubarych, *J. Opt. Soc. Am. B*, 2010, **27**, 3, 382.

[8] T. Brixner, T. Mančal, I. V. Stiopkin, and G. R. Fleming, *J. Chem. Phys.*, 2004, **121**, 9, 4221-4236.

[9] A. Iagatti *et al.*, *J. Phys. Chem. C*, 2015, **119**, 35, 20256-20264.

[10] D. R. Tackley, D. Geoffrey, and W. E. Smith, *Phys. Chem. Chem. Phys.*, 2001, **3**, 1419-1426.

[11] S. Hoyer, M Sarovar, and K, B. Whaley, *New J. Phys.*, 2010, **12**.

[12] J. R. Caram, S. Doria, D. M. Eisele, F. S. Freyria, T. S. Sinclair, P. Rebentrost, S. lloyd, and M. G. Bawendi, *ACS Nano*, 2016, **16**, 11, 6808-6815

[13] V. Czikkely, H. D. Forsterling, and H. Khun, *Chem. Phys. Lett.*, 1970, **6**, 3, 207-210.

[14] G. D. Scholes, *Annu. Rev. Phys. Chem.*, 2002, **54**, 57–87.